Nanoconfined Atomic Layer Deposition of TiO_2/Pt Nanotubes: Toward Ultrasmall Highly Efficient Catalytic Nanorockets

Jinxing Li, Wenjuan Liu, Jiyuan Wang, Isaac Rozen, Sha He, Chuanrui Chen, Hyun Gu Kim, Ha-Jin Lee, Han-Bo-Ram Lee, Se-Hun Kwon, Tianlong Li, Longqiu Li, Joseph Wang,* and Yongfeng Mei**

Small machines are highly promising for future medicine and new materials. Recent advances in functional nanomaterials have driven the development of synthetic inorganic micromachines that are capable of efficient propulsion and complex operation. Miniaturization and large-scale manufacturing of these tiny machines with true nanometer dimension are crucial for compatibility with subcellular components and molecular machines in operation. Here, block copolymer lithography is combined with atomic layer deposition for wafer-scale fabrication of ultrasmall coaxial TiO_2/Pt nanotubes as catalytic rocket engines with length below 150 nm and a tubular reactor size of only 20 nm, leading to the smallest man-made rocket engine reported to date. The movement of the nanorockets is examined using dark-field microscopy particle tracking and dynamic light scattering. The high catalytic activity of the Pt inner layer and the reaction confined within the extremely small nanoreactor enable highly efficient propulsion, achieving speeds over 35 µm s^{-1} at a low Reynolds number of <10^{-5}. The collective movements of these nanorockets are able to efficiently power the directional transport of significantly larger passive cargo.

1. Introduction

Through millions of years of evolution, nature represents a treasure trove of highly efficient biomolecular motors that are used in different biological processes, such as intracellular transport and macroscale muscular actuation.[1,2] Recent advances in functional organic and inorganic nanodevices have driven the development of synthetic micro- and nanomachines that are capable of efficient propulsion and complex operation at the nanoscale.[3–7] A myriad of natural and synthetic molecular motors, rotors, and ratchets have been utilized at this scale to power nano-electrical-mechanical systems,[8,9] exert torques,[10] switch molecular logic gates,[11] or nanomanipulate individual molecules.[12] Meanwhile, on a relatively larger scale, researchers have developed micrometer-sized structures that can achieve autonomous chemically powered propulsion for diverse applications ranging from drug delivery[13] to environmental remediation.[14] Shrinking the dimensions of these small self-propelled swimmers to the true nanometer scale is crucial for compatibility with subcellular components and synthetic molecular devices, but has seldom been investigated.[15–18]

Swimming in low Reynolds number environments has been realized through different propulsion mechanisms, such as self-diffusiophoresis,[19,20] self-electrophoresis,[21] and bubble thrust.[22] These propulsion mechanisms commonly utilize asymmetric catalytic surface reactions of chemical fuels to generate directed motion. However, because rotational diffusivity dramatically increases upon decreasing the swimmer dimension, randomizing Brownian forces heavily disrupt directional motion. Microscale rockets, characterized by their use of bubble propulsion, are capable of overcoming the strong randomizing Brownian forces to propel efficiently in real-life media, and are thus among the most powerful synthetic micromachines to date.[23–26] Therefore, tubular rockets represent one of the most attractive designs for creating efficient nanoscale swimmers. Generally, such microrockets consist of hollow tubular catalytic reactors (typically 5–200 µm long and 2–20 µm in diameter)

J. Li, Dr. W. Liu, I. Rozen, S. He, C. Chen, T. Li, Prof. J. Wang
Department of Nanoengineering
University of California San Diego
La Jolla, CA 92093, USA
E-mail: josephwang@ucsd.edu
J. Wang, Dr. T. Li, Prof. L. Li
State Key Laboratory of Robotics and System
Harbin Institute of Technology
Harbin, Heilongjiang 150001, P. R. China
E-mail: longqiuli@hit.edu.cn
H. G. Kim, Prof. H.-B.-R. Lee
Department of Materials Science and Engineering
Incheon National University
Incheon 22012, Republic of Korea
H.-J. Lee, Prof. S.-H. Kwon
School of Materials Science and Engineering
Pusan National University
Busan 46241, Republic of Korea
Prof. Y. F. Mei
Department of Materials Science
Fudan University
Shanghai 200433, P. R. China
E-mail: yfm@fudan.edu.cn

DOI: 10.1002/adfm.201700598

which are commonly prepared by template electrodeposition or rolled-up nanotechnology techniques.[27–29] However, realizing a nanoscale reactor with a tubular catalytic engine is extremely challenging because 3D anisotropic structures with a well-defined cavity and materials composition are difficult to synthesize in high yield and with good structural fidelity by either conventional photolithography or wet-chemistry electrosynthesis methods.

In this work, block copolymer lithography is used to create well-defined nanopores which confine the atomic layer deposition (ALD) of TiO_2/Pt nanotubes for use as extremely small nanorockets. Block copolymer lithography represents an attractive alternative patterning technology over photolithography due to its ability to produce highly periodic and ordered subdiffraction nanostructures via self-assembly on length scales ranging from few to hundreds of nanometers.[30–33] ALD is a thin film deposition technique capable of highly conformal growth, utilizing cycles of self-limiting surface reactions of alternating precursors for uniform layer thicknesses with atomic level control.[34–36] By combining the capabilities of block copolymer lithography and ALD, the presented high-throughput fabrication technique overcomes all of the aforementioned challenges for creating extremely small and efficient nanoscale rocket engines, which represent the most significant miniaturization of catalytic nanoengines reported to date.[23–26] The fabricated structures, with lengths of 120–150 nm, contain a hollow Pt-coated cylindrical chamber with size down to 20 nm. The resulting Pt nanotubes catalyze the decomposition of hydrogen peroxide fuel to water and oxygen, producing a strong local oxygen gradient for efficient self-diffusiophoretic propulsion. Combining finite element method simulations with an analytical model of their self-diffusiophoretic propulsion shows that the tubular nanotube design of the new nanorockets offers much more efficient hydrodynamic interactions than nanowire motors or Janus nanosphere motors of similar dimensions. As proof of concept, the collective motion of these nanorockets is used to actuate passive microparticles for directional cargo transport.

2. Results

Figure 1 details the fabrication process of the nanoconfined atomic layer deposition of the TiO_2/Pt nanotubes. The fabrication begins with block copolymer lithography to prepare the cylindrical nanopores that serve as the nanorocket templates, which are subsequently coated with thin films via atomic layer deposition. A 150 nm film of epoxy-based SU8 photoresist, used to define the nanorocket length, is first spin-coated onto a Si wafer and exposed to ultraviolet light for the crosslinking reaction. Subsequently, a 40 nm thick film of the silicon-containing diblock copolymer, polystyrene-block-poly(4-(*tert*-butyldimethylsilyl)oxystyrene) ($PS_{31.0k}$-*b*-$PSSi_{69.7k}$), is spin-coated over the SU8 layer (Figure 1A). This bilayer structure is then annealed in a mixed heptane–toluene solvent vapor (volume ratio $V_{hep}/V_{tol} = 4$) at 25 °C, which induces rearrangement of the copolymer film into PS cylindrical nanodomains oriented perpendicular to the substrate in a PSSi matrix, shown in Figure 1B.[37] These PS cylinders have diameters of 60 nm and are arranged in a hexagonal pack uniformly across the substrate; other template geometries and dimensions are possible under different solvent vapor annealing conditions.[38] This block polymer film is then etched via anisotropic oxygen reactive-ion etching (RIE), removing the organic block and the

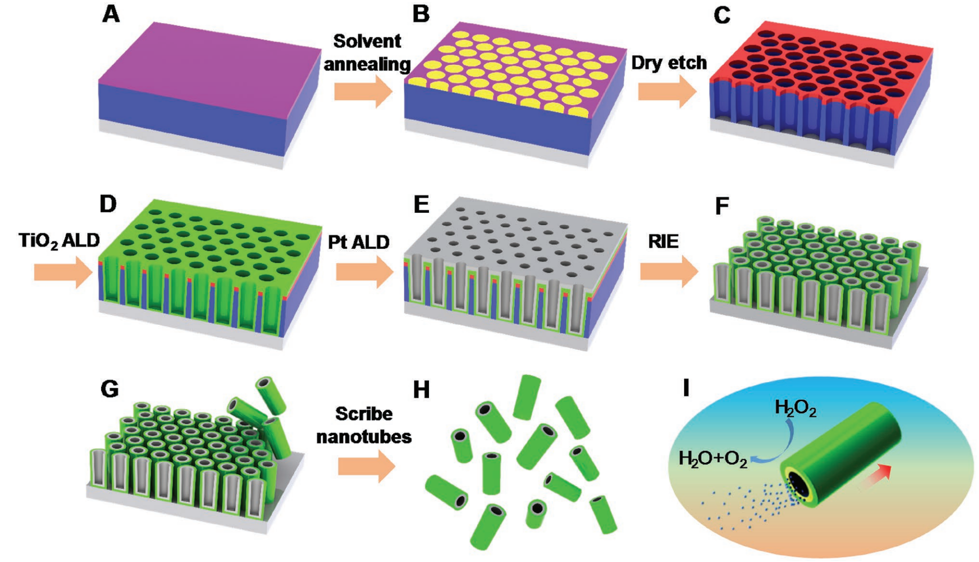

Figure 1. Schematic of nanoconfined atomic layer deposition (ALD) of TiO_2/Pt nanorockets. A) A thin film of PS-*b*-PSSi is first spin-coated over a crosslinked film of SU8 on a Si wafer. B) Subsequent solvent vapor annealing yields vertically aligned hexagonal packed cylindrical PS nanodomains. C) Dry etching of the PS and underlying SU8 produces 60 nm diameter pores. D) Conformal thin film of TiO_2 by ALD for the outer rocket shell. E) ALD of a conformal thin film of Pt by ALD for the inner rocket layer, leaving a small inner 20 nm tubular nanotube. F) Reactive ion etching and calcining removes the overlayers and outer template walls. G,H) Lift-off yields nanorockets with an exposed hollow Pt nanoreactor inside the TiO_2 outer shell. I) Decomposition of H_2O_2 at the Pt nanoreactor generates a strong local O_2 gradient for efficient self-diffusiophoretic propulsion, the arrow indicates the moving direction of the rocket.

cylindrical PS fillings, leaving behind a porous SiO_2 matrix (Figure 1C). The exposed SU8 layer is subsequently etched to expose the Si wafer, yielding the nanorocket template consisting of a dense array of coaxial nanotubes.

Low-temperature ALD is used to deposit a thin conformal coating of TiO_2 over the template to serve as robust nanoscale cavities (Figure 1D). The TiO_2 layer is deposited at 150 °C using a pulse sequence of titanium isopropoxide (TTIP, DNF solution) and H_2O precursors. A TiO_2 thickness of 15 nm is obtained at 400 cycles. This conformal deposition into the nanopores produces the mildly conical nanorocket shell. The deposition of a catalytic layer inside the nanoreactor, crucial to nanorocket propulsion, is accomplished by coating the nanoreactor with Pt with a thickness of 5 nm (Figure 1E), through a thermal O_2-based ALD process using the (1,2,5,6-η)-1,5-hexadienedimethylplatinum(II) (HDMP) precursor at a temperature of 100 °C.[39] Subsequently, Cl_2 RIE and CF_4 DRIE are used to etch back the platinum and TiO_2 overlayers, respectively, and to polish and planarize the surface, exposing the SiO_2 matrix layer. The sample is then calcined at 500 °C in air for 4 h to remove the interstitial SiO_2 matrix and underlying SU8 layer, leaving behind upright and separated TiO_2/Pt nanotubes attached to the sample wafer (Figure 1F). Lift-off is accomplished by separating the TiO_2 ends from the wafer by mechanical scribing (Figure 1G,H), resulting in well-defined TiO_2/Pt nanorockets with uniform dimensions which can self-propel in H_2O_2 fuel (Figure 1I).

Figure 2 displays scanning electron microscopy (SEM) images corresponding to the intermediate fabrication steps of the nanorockets. Figure 2A shows the dense and highly ordered hexagonal arrangement of the polymer template. Figure 2B,C, taken after the TiO_2 and Pt ALD procedures, respectively, shows the decreased diameter of the individual nanotubes following conformal growth of the two layers. SEM image of the nanorockets attached to the wafer after RIE and calcination is shown in Figure 2D. A tilted close-up of the sample (Figure 2E) with a strong contrast of the two layers confirms the bilayer nanocavities with slightly conical openings, which facilitates the fuel entry into the nanoreactor. A larger view of sample in Figure 2F shows the uniformity of the fabricated nanorockets. The yield of this polymer lithography-assisted procedure is 1.96×10^{10} nanorockets cm^{-2} of sample wafer. Therefore, the template-confined ALD process represents a highly reliable and efficient technology for high throughput fabrication of uniform nanorockets with nanometer resolution.

The structure of the nanorocket and the materials compositions are characterized using transmission electron microscopy (TEM) and X-ray diffraction (XRD) in **Figure 3**. The micrograph in Figure 3A shows a group of released TiO_2/Pt nanorockets, illustrating the homogeneity in their shapes and dimensions. These images reveal the well-defined nanoconical TiO_2 outer shape with a slightly larger opening to a hollow Pt chamber and a sharp taper at the narrow end, representing the original point of attachment to the Si wafer. This nanoconical shape with a wide opening diameter facilitates fuel entry into the nanoreactor for highly efficient propulsion, while the flat exterior further reduces the viscous drag on the nanorocket body. The TEM image of Figure 3B displays a single representative TiO_2/Pt nanorocket, clearly illustrating the separate layer components. This directly shows that the low-temperature ALD processes produce a stable TiO_2 nanotube which supports a conformal and uniform interior Pt coating. The outer TiO_2 layer of the nanorocket is measured to be ≈15 nm thick, the Pt inner layer to be ≈5 nm thick, while the hollow chamber's size to be 10–20 nm, with the nanorocket length to be 120–150 nm. To the best of our knowledge, this design represents the smallest man-made engine with a tubular or conical shape. The effect of the geometric dimensions of tubular micro/nanomotors, such as diameter and length, on their speed has been thoroughly studied in our previous work.[40] In general, the nanorocket speed is dependent on the propulsive force associated with the chemical reaction and on the viscous drag forces acting on the nanorocket. Larger catalytic surface areas can contribute to larger propulsive forces, but larger sizes also increase the viscous drag force. In our present design with such a small dimension, the thickness of both the TiO_2 and Pt layer is relatively thin to ensure a larger inner catalytic surface area, while the nanotube with a 120–150 nm length could help to reduce the viscous force for efficient propulsion. The XRD patterns of the nanorockets sample in Figure 3C correspond to TiO_2 and TiO_2 + Pt. Scanning TEM electron energy loss spectroscopy (STEM-EELS) elemental maps confirm the elemental composition and distributions of the nanorockets (Figure 3D–F).

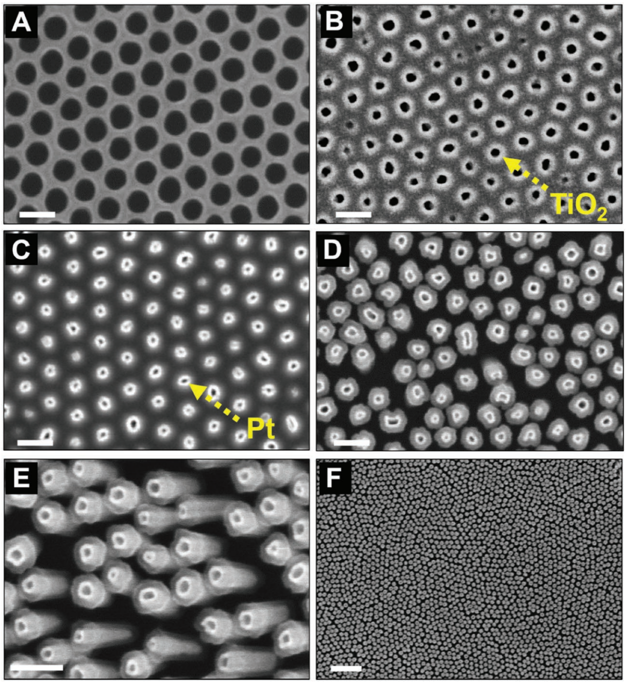

Figure 2. SEM characterization of nanorocket fabrication. A) The polymer template with a hexagonal array of cylindrical pores. B) ALD of TiO_2 (15 nm) in the nanopores as the outer layers of the nanorockets. C) ALD of Pt (5 nm) in the nanopores as the inner layers of the nanorockets. D) Reactive ion etching and calcining removes the overlayers and template walls, respectively, leaving separated nanorockets attached to the wafer. E) Tilted cross-sectional close-up view of the attached nanorockets. F) Enlarged view of nanorocket array on the wafer. Scale bars: A–E) 100 nm; F) 500 nm.

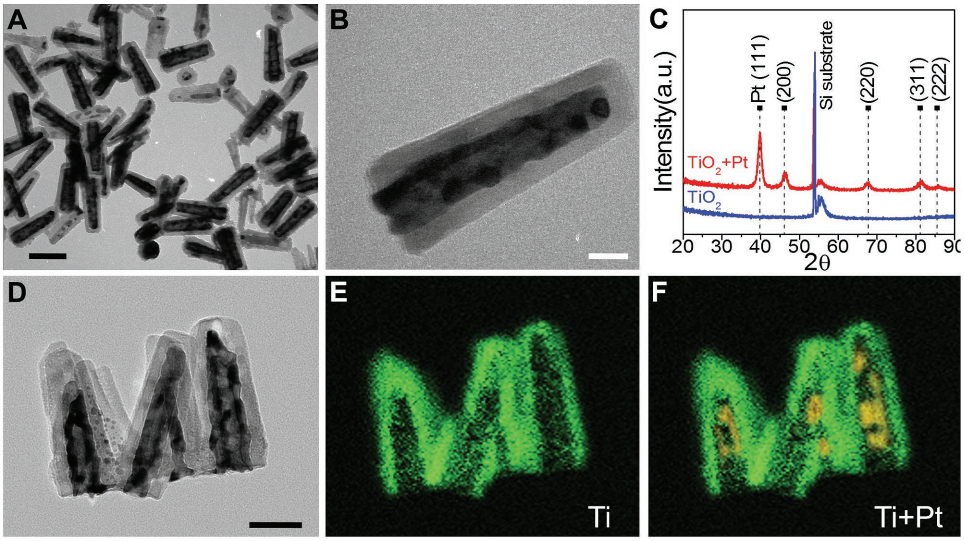

Figure 3. Characterization of nanorockets. TEM images of A) a group of TiO_2/Pt nanorockets and B) a zoom-in single nanorocket, showing the mildly conical structure of the nanorocket. C) XRD pattern of the TiO_2/Pt nanorockets. D) TEM image and STEM-EELS elemental maps of E) Ti and F) Ti + Pt. Scale bars: A) 100 nm; B) 20 nm; D–F) 50 nm.

The resulting TiO_2/Pt nanorockets can achieve highly efficient autonomous propulsion in the presence of hydrogen peroxide fuel (**Figure 4**). Principally, the exposed inner Pt surface in the nanorocket engine catalyzes the decomposition of H_2O_2 fuel into H_2O and O_2 as follows: $2H_2O_2 \xrightarrow{\text{Pt}} 2H_2O + O_2$. Other fuels, such as hydrazine, glucose, and urea, may be used to achieve similar chemically powered motion in conjunction with an appropriate catalytic or biocatalytic surface.[41–43] A dark-field optical microscope coupled with a charge-coupled device (CCD) camera is able to perform real-time tracking of particles of size 30–1000 nm, enabling observation of the dynamic behavior of nanorockets. Figure 4A displays the representative trajectories over 6 s period of a TiO_2/Pt nanorocket undergoing Brownian motion in the absence of fuel, while Figure 4B depicts the representative trajectories of a TiO_2/Pt nanorocket undergoing efficient propulsion in the presence of 15% H_2O_2 fuel (see Movie S1 in the Supporting Information). It is observed that the nanorockets exhibit highly constrained motion without fuel, whereas the nanorockets with the fuel show highly efficient movement, with propulsion lifetimes lasting upward of 60 min. These observations suggest that regardless of extremely small nanorocket size, the nanoconfined catalytic reaction in the tubular reactor can efficiently convert chemical energy into mechanical motion over long durations.

Based on the dark-field microscopy tracking, the average mean squared displacements of nanorockets as a function of time can be plotted for each different level of fuel, including 0% (without fuel) as a control (Figure 4C). The displacement data were acquired by individual nanorocket-tracking analysis as used above for samples of nanomotors ($n > 30$) moving in the presence of three different fuel concentrations (5%, 10%, and 15%) over short time scales. The mean squared displacement of the nanorockets is obtained using the self-diffusiophoretic model,[20] where the directional motion of self-propelled particles is governed by a ballistic parabolic component for short time and a diffusive linear component at long time. Using the characteristic equations, the effective translational diffusion coefficients D_{eff} of a nanorocket from the slope $D_{\text{eff}} = \frac{\text{MSD}}{4t}$ can be derived over sufficiently long time periods. In the absence of fuel (green line in Figure 4C), the experimental mean square displacement (MSD) plot is linear and that $D_{\text{eff}} = 6.45\ \mu m^2\ s^{-1}$, consistent with the expected diffusion coefficient of a particle undergoing typical Brownian motion. In the presence of fuel, the nanorocket MSD plots become parabolic within 1 s, reflecting the ballistic trajectory due to the self-propulsion and the reorientation due to rotational diffusion, respectively. Increasing the fuel concentration to 5%, 10%, and 15% results in larger effective diffusion coefficients of 13.3, 30.5, and 51.4 $\mu m^2\ s^{-1}$, respectively, indicating that the self-propulsion in the catalytically active Pt chamber is primarily responsible for the enhanced diffusion of the nanorockets.

Dynamic light scattering (DLS) measurements are performed to capture the hydrodynamic size distribution of these nanorockets (Figure 4D). The nanorocket's hydrodynamic size is inversely related to the previously determined translational diffusion coefficients, as given by the Stokes–Einstein equation $D_{\text{eff}} = \frac{Tk_b}{3\pi\eta d}$, where $k_b T$ is the thermal energy, η is kinematic viscosity, and d is the hydrodynamic diameter. The average hydrodynamic diameter of the nanorockets in the absence of fuel is 88 nm (see green curve in Figure 4D), which reflects motion solely under the effects of Brownian diffusion. The addition of 15% fuel results in a smaller average hydrodynamic diameter of 33.7 nm (red curve), corresponding to a D_{eff} of 14.6 $\mu m^2\ s^{-1}$, which is consistent with the result obtained by single particle tracking. Here, when the nanorockets self-propel in the presence of fuel, the accelerated random walk trajectory and the correspondingly greater D_{eff} causes the apparent sizes of the nanorockets to decrease, in agreement with the enhanced diffusion coefficients derived in the MSD measurements. These DLS measurements provide concrete evidence that the majority of nanorockets display a highly efficient motion, beyond the manually tracked individuals.

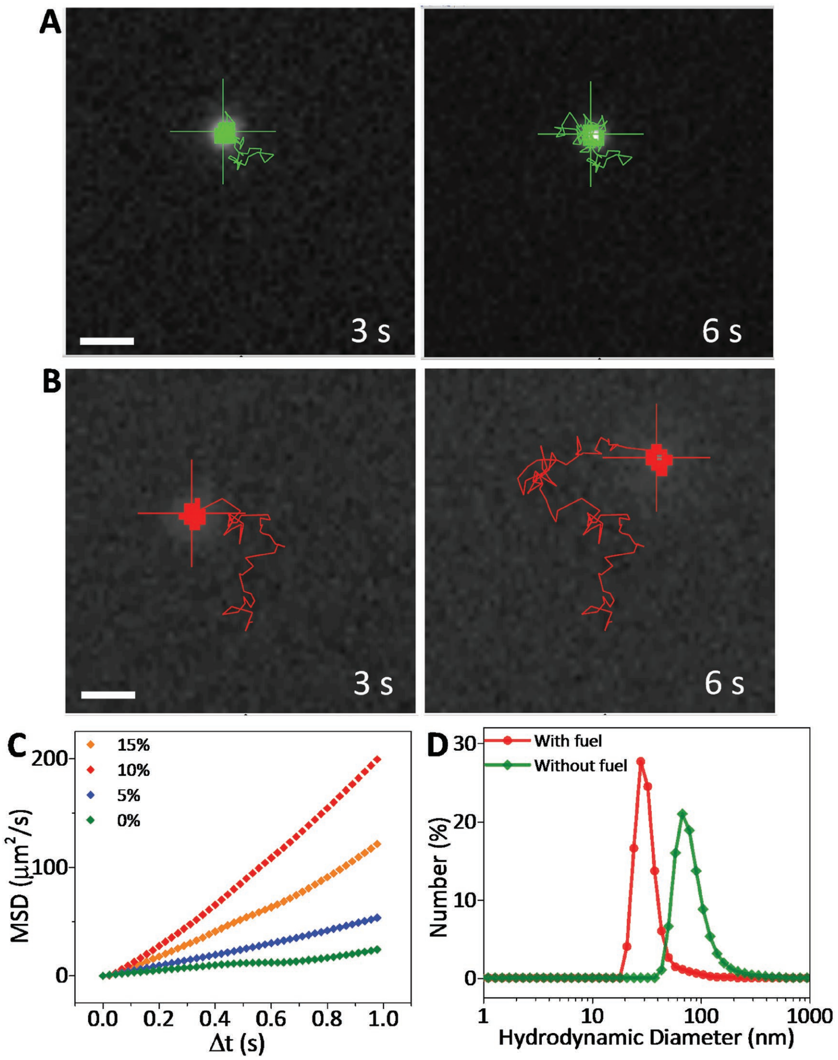

Figure 4. Propulsion performance at different fuel conditions. Dark-field microscopy video frames and trajectories (from Movie S1, Supporting Information) displaying track lines of motion over 6 s of an individual nanorocket moving in the A) absence and B) presence of 15% H_2O_2 fuel. Scale bar: 300 nm. C) Average mean square displacement (MSD) as a function of time interval for nanorockets ($n > 30$) moving in the presence of H_2O_2 fuel with different concentrations over 1 s. D) Nanorocket size distribution as measured by dynamic light scattering, in the presence of 0% (green) and 15% (red) H_2O_2 fuel, respectively.

Figure 5A displays the nanorocket speed dependence on the H_2O_2 concentration. It is observed that with a fuel concentration of 15%, the nanorocket could reach speeds over 35 µm s^{-1} at a low Reynolds number of $<10^{-5}$. As no bubbles were observed in the experiments while the Pt/TiO_2 composition cannot support the necessary self-generated electric field, we assume the high speed of the nanorockets is resulted from the strong self-diffusiophoretic propulsion.[44] Based on the self-diffusiophoretic propulsion model,[44] the diffusiophoretic force is highly related to the local chemical gradient. Figure 5B displays the simulated O_2 concentration distribution produced by a tubular nanorocket undergoing self-diffusiophoresis. It is observed that a strong oxygen gradient is generated at the opening of the nanorocket reaction chamber, leading to an oxygen gradient up to 10^7 mol m^{-4}. Because of the larger Pt catalyst surface area and nanoconfinement of the nanorockets, a very high O_2 diffusion flux and corresponding diffusiophoretic force are generated, leading to an efficient nanorocket propulsion. Because of the larger catalytic Pt surface area and the tubular structure of the nanorockets, a much higher O_2 diffusion flux and corresponding diffusiophoretic force are generated, leading to a much more efficient propulsion compared to cylindrical and spherical motors with equivalent dimensions. As the nanotubular reactor of the nanorockets confers the largest catalytic surface area and produces a strongly defined direction of diffusion, the local concentration gradient around the catalytic surface is larger for the tubular motor than for the other geometries, corresponding to a higher O_2 diffusion flux and to a much higher speed.

Collective behavior driven by a uniform response to an external field is a notable characteristic of biological and artificial micro- and nanomotors,[45–49] with the self-organization driven by local interactions between individual motors in the assembly and the environment. In particular, the collective motion of self-propelled swimmers due to an imposed chemical gradient is a rich topic because of the complexities introduced by the interplay between self-propulsion, Brownian motion, and chemotactic effects. This behavior has been applied in active transport phenomena,[46] chemotactic search strategies,[47,48] and nanomachinery.[10] Inspired by these efforts, the collective motion of the fabricated nanorockets, with a very high concentration in the suspension, is also investigated. The fuel concentration dependence of the catalytic swimmer on their velocities can promote chemotactic migration toward higher fuel concentration in the presence of an imposed peroxide gradient.[49] The scheme in Figure 5C illustrates how this net nanorocket flux is used to achieve large-scale directed transport of passive cargos, where individual nanorockets accumulate along the side of the tracer and move the tracer with their collective thrust. The time-lapse white-light microscopy images in Figure 5C, corresponding to Movie S2 (Supporting Information), shows the apparent movement of passive 5 µm SiO_2 particles over 12 s due to the nanorocket chemotactic motion in the presence of an imposed peroxide gradient in a sealed cell (see the Experimental Section). Free nanorockets move further along the gradient than against it due to their increasing speed, resulting in net diffusion toward regions of higher fuel concentration during their enhanced random walk trajectory.[50] However, the introduction of the large tracer particle introduces a barrier in these trajectories, causing the swimming nanorockets to lock against the tracer surface until a tumble event reorients the nanorocket. For

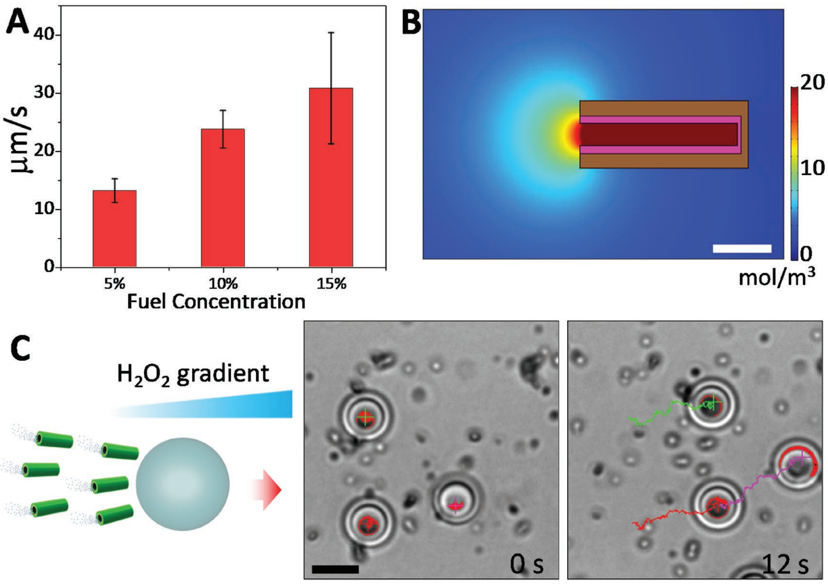

Figure 5. Propulsion simulations and collective behavior. A) Nanorocket speed as a function of the H_2O_2 concentration ($n = 30$). B) Simulation of oxygen concentration distribution produced by the tubular bilayer nanorocket in the presence of 15% H_2O_2 fuel. Pt is indicated as pink; TiO_2 is indicated as brown. Scale bar: 60 nm. Right: Schematic of the rocket design and related fuel reactions. C) Schematic illustration of nanorocket propulsion under an imposed fuel gradient for transporting larger passive microscale objects. Time-lapse microscopy images show the displacement of a passive SiO_2 microsphere over 12 s (from Movie S2, Supporting Information), driven by a group of TiO_2/Pt nanorockets in an imposed peroxide gradient (H_2O_2 source is on the right of the images). Scale bar: 5 µm.

sparse swimming nanorockets, the reorientation is quick and minimizes any pushing force, but in concentrated suspensions, local packing effects at the tracer surface reduce the nanorocket attrition and promote significant thrust at the surface, resulting in net movement along the concentration gradient. The tracers do not have a random walk trajectory, as symmetry cancels out net motion normal to the gradient, while the nanorocket chemotactic effects result in a net thrust toward the higher fuel concentrations, leading to an approximately linear observed tracer motion. Control of such fuel gradients could allow for these nanorocket active suspensions to effectively transport large passive colloids or target analytes toward specific sites, or power nanomachinery through applied torques.

3. Conclusion

A wafer-scale synthesis method has been used for the fabrication of well-defined nanorockets composed of a TiO_2 tubular structure enclosing a Pt catalytic nanoreactor, through the combination of block copolymer lithography with atomic layer deposition. The resulting nanorockets represent the most significant miniaturization of catalytic tubular engines reported to date, displaying attractive propulsion performance at substantially smaller length scales associated with much lower Reynolds number and stronger Brownian fluctuation. Their highly efficient propulsion via the catalytic decomposition of hydrogen peroxide fuel in the 20 nm nanoreactor results in high speeds of ≈35 µm s^{-1}, as experimentally verified through dark-field microscopy particle tracking and dynamic light scattering measurements. The self-propelling nanorockets undergo directed motion via chemotaxis in a controlled H_2O_2 gradient, which can be used to transport much larger passive tracers. The highly versatile fabrication strategy can be readily adapted for mass-production of high-quality nanorockets for fundamental research toward understanding the nonequilibrium nanoscale dynamics, as well as broad practical implications such as individual nanomanipulation of enzymes, proteins, and other macromolecules.

4. Experimental Section

Fabrication of Nanorockets: Initially, 150 nm thick crosslinked SU-8 films were prepared by using ultraviolet light exposure on coated SU-8 films to define the nanorocket length. And then, a 40 nm film of PS-*b*-PSSi (PS$_{31.0k}$-*b*-PSSi$_{69.7k}$) having the molecular weights of 31 000 g mol^{-1} for PS and 69 700 g mol^{-1} for PSSi blocks was sequentially spin-coated onto the crosslinked SU-8 film. This bilayer structure was annealed for 4 h in a mixed heptane–toluene solvent vapor with a volume fraction of V_{hep}/V_{tol} = 4 at a room temperature. Solvent annealing resulted in highly ordered arrays of PS cylindrical patterns oriented perpendicular to the substrate surface and embedded in the PSSi matrix. This block polymer film was then etched via anisotropic oxygen RIE, removing the organic block and the cylindrical PS fillings, leaving behind a porous SiO_2 matrix. The exposed SU-8 layer was subsequently etched to expose the Si wafer, yielding the nanorocket template consisting of a dense array of coaxial nanotubes.

Low-temperature ALD was then used to deposit a thin conformal coating of TiO_2 over the template. The TiO_2 layer was deposited at 150 °C using a pulse sequence of TTIP, DNF solution and H_2O precursors. A TiO_2 thickness of 10 nm was obtained at 400 cycles. This conformal deposition into the nanopores produced the mildly conical nanorocket shell. The deposition of a catalytic layer inside the nanoreactor crucial to nanorocket propulsion was accomplished by coating the nanoreactor with Pt with a thickness of 5 nm, through a thermal O_2-based ALD process using HDMP precursor at a temperature of 100 °C. Subsequently, Cl_2 RIE and CF_4 DRIE were used to etch back the platinum and TiO_2 overlayers, respectively, and to polish and planarize the surface, exposing the SiO_2 matrix layer. The sample was then calcined at 500 °C in air for 4 h to remove the interstitial SiO_2 matrix and underlying SU-8 layer, leaving behind upright and separated TiO_2/Pt nanotubes attached to the sample wafer. Lift-off was accomplished by separating the TiO_2 ends from the wafer by mechanical scribing, resulting in well-defined TiO_2/Pt nanorockets with generally uniform dimensions. All nanorockets were stored in ultrapure water (18.2 MΩ cm) at room temperature and tested prior to each experiment to verify their motion capabilities.

Nanorocket Material Composition Analysis: SEM images were obtained with a Phillips XL30 ESEM instrument, using an acceleration potential of 20 kV. Cross-sectional images were obtained by tilting the samples by 45°. Individual nanorockets were also studied by high-resolution TEM (JEOL JEM-ARM200F). XRD studies were measured with a model RIGAKU D/MAX-2500. Elemental mapping was conducted on Tecnai G2 Polara microscope equipped with a field emission gun (Accelarating voltage 300 kV).

Propulsion Experiments: Aqueous H_2O_2 solutions (H325-500, Fisher) with concentrations ranging from 10% to 30% were prepared. Dark-field microscopy videos were taken on a Zeiss AxioObserver. Z1 inverted microscope with an attached Basler acA2000-340kc camera. A 1 μL droplet containing the nanorockets was placed first on a glass slide. Afterward, a 1 μL droplet of peroxide solution was mixed directly into the nanorocket droplet. Videos were taken at a frame rate of 45 frames per second. A 40× objective (numerical aperture, NA = 0.75) coupled with a dark field condenser (NA = 1.2/1.4) was used to collect light scattered from the nanorockets. Particle tracking was subsequently performed in Metamorph to capture the average nanorocket speed for each nanorocket sample. Samples of 30 nanorockets at each fuel concentration were individually tracked for their mean squared displacements over 1 s. Primarily, tracking was performed manually due to the low contrast in the videos.

Dynamic Light Scattering Measurements: Dynamic light scattering measurements were conducted using a Malvern Zetasizer Nano Z with 40 μL disposable microcuvettes. Nanorocket solutions in the presence of 1×10^{-3} M sodium citrate were filtered with a syringe filter (Whatman FP 30/0.2, pore size 0.2 μm). The appropriate amount of H_2O_2 was added prior to the DLS experiments, yielding solutions with 15% H_2O_2 or no fuel. Sonication was briefly used to remove any gas bubbles formed if necessary. The instrument scattering angle is 173°. DLS data were processed using a Dispersion Technology Software (Malvern Instruments).

Transport Experiments: Experiments were conducted in a Dunn chemotaxis cell (Hawksley, UK). First, a mixture of nanorockets and 5 μm PS particles (Bangs Laboratories, Fisher, IN, USA) was dispersed in water in the inner well, and the outer well was filled with water. A thick coverslip was seeded with the particle solution, and placed over the wells and bridge, leaving a minor gap of the outer well. A wax mixture was then applied to seal the coverslip in place. Then, the outer well was drained through the exposed slit and replaced with a 15% hydrogen peroxide solution (w/v). The gap was subsequently sealed. Videos were captured by an inverted optical microscope (Nikon Instrument Inc. Ti-S/L100), coupled with a 40× objective and a Hamamatsu digital camera C11440 using the NIS-Elements AR 3.2 software.

Numerical Analysis: Multiphysics software (COMSOL Inc., Burlington, MA) was used to simulate the concentration distribution due to the O_2 molecular diffusion around each of the three catalytic nanomotor geometries, using the Transport of Diluted Species interface. First, the catalytic surfaces of the nanomotors were chosen as the inflow boundary of the O_2 molecule diffusion, and the value of the concentration was set to 750 mol m^{-3}. The diffusion coefficient of the O_2 was set to 2.42×10^{-9} m^2 s^{-1}. Then, the mesh was set to Free Triangular, with the max and min sizes set to 1 and 0.1 nm, respectively. The O_2 molecular diffusion concentration nephograms and the corresponding gradient nephograms for each geometry were obtained at a running time over 0–10^{-5} s, with a time step of 1×10^{-6} s. From the centerline along the axis of each nanomotor, linear profiles of the O_2 concentration gradient over 50 nm were obtained.

Supporting Information

Supporting Information is available from the Wiley Online Library or from the author.

Acknowledgements

The Pt ALD was supported by the Basic Science Research Program through the National Research Foundation of Korea (NRF) funded by the Ministry of Education (2014R1A1A2059845). This work was supported by the Global Frontier R&D Program (2013-073298) on Center for Hybrid Interface Materials (HIM) funded by the Ministry of Science, ICT & Future Planning. W.L., C.C., and T.L. acknowledge the China Scholarship Council (CSC) for the financial support. This work was performed in part at the San Diego Nanotechnology Infrastructure (SDNI), a member of the National Nanotechnology Coordinated Infrastructure, which is supported by the National Science Foundation (Grant ECCS-1542148). Y.F.M. acknowledges the Natural Science Foundation of China (U1632115), the National Key Technologies R&D Program of China (2015ZX02102-003) and the Changjiang Young Scholars Programme of China.

Conflict of Interest

The authors declare no conflict of interest.

Keywords

atomic layer deposition, block polymer nanolithography, catalytic propulsion, collective behavior, nanorockets

Received: February 2, 2017
Revised: March 15, 2017

---

[1] J. Howard, *Mechanics of Motor Proteins and the Cytoskeleton*, Sinauer, Sunderland, MA **2001**.
[2] M. Schliwa, G. Woehlke, *Nature* **2003**, *422*, 759.
[3] C. Montemagno, G. Bachand, *Nanotechnology* **1999**, *10*, 225.
[4] M. G. Van den Heuvel, C. Dekker, *Science* **2007**, *317*, 333.
[5] J. Wang, *ACS Nano* **2009**, *3*, 4.
[6] J. Wang, *Nanomachines: Fundamentals and Applications*, Wiley-VCH, Weinheim **2013**.
[7] W. Wang, W. Duan, S. Ahmed, T. E. Mallouk, A. Sen, *Nano Today* **2013**, *8*, 531.
[8] R. K. Soong, G. D. Bachand, H. P. Neves, A. G. Olkhovets, H. G. Craighead, C. D. Montemagno, *Science* **2000**, *290*, 1555.
[9] H. Hess, G. D. Bachand, V. Vogel, *Chem. Eur. J.* **2004**, *10*, 2110.
[10] R. Di Leonardo, L. Angelani, D. Dell'Arciprete, G. Ruocco, V. Iebba, S. Schippa, M. P. Conte, F. Mecarini, F. De Angelis, E. Di Fabrizio, H. C. Berg, *Proc. Natl. Acad. Sci. USA* **2010**, *107*, 9541.
[11] I. Willner, B. Shlyahovsky, M. Zayats, B. Willner, *Chem. Soc. Rev.* **2008**, *37*, 1153.
[12] B. Lewandowski, G. De Bo, J. W. Ward, M. Papmeyer, S. Kuschel, M. J. Aldegunde, P. M. E. Gramlich, D. Heckmann, S. M. Goldup, D. M. D'Souza, A. E. Fernandes, D. A. Leigh, *Science* **2013**, *339*, 189.
[13] J. Wang, W. Gao, *ACS Nano* **2012**, *6*, 5745.
[14] L. Soler, S. Sánchez, *Nanoscale* **2014**, *6*, 7175.
[15] X. Ma, A. C. Hortelao, A. Miguel-López, S. Sánchez, *J. Am. Chem. Soc.* **2016**, *138*, 13782.
[16] D. A. Wilson, R. J. Nolte, J. C. van Hest, *Nat. Chem.* **2012**, *4*, 268.
[17] T. C. Lee, M. Alarcón-Correa, C. Miksch, K. Hahn, J. G. Gibbs, P. Fischer, *Nano Lett.* **2014**, *14*, 2407.
[18] M. Enachi, M. Guix, V. Postolache, V. Ciobanu, V. M. Fomin, O. G. Schmidt, I. Tiginyanu, *Small* **2016**, *12*, 5497.
[19] W. F. Paxton, S. Sundararajan, T. E. Mallouk, A. Sen, *Angew. Chem. Int. Ed.* **2006**, *45*, 5420.
[20] J. R. Howse, R. A. Jones, A. J. Ryan, T. Gough, R. Vafabakhsh, R. Golestanian, *Phys. Rev. Lett.* **2007**, *99*, 048102.
[21] Y. Wang, R. M. Hernandez, D. J. Bartlett, J. M. Bingham, T. R. Kline, A. Sen, T. E. Mallouk, *Langmuir* **2006**, *22*, 10451.
[22] W. Gao, S. Sattayasamitsathit, J. Orozco, J. Wang, *J. Am. Chem. Soc.* **2011**, *133*, 11862.
[23] Y. Mei, G. Huang, A. A. Solovev, E. B. Urena, I. Monch, F. Ding, T. Reindl, R. K. Y. Fu, P. K. Chu, O. G. Schmidt, *Adv. Mater.* **2008**, *20*, 4085.

[24] A. A. Solovev, Y. Mei, E. B. Urena, G. Huang, O. G. Schmidt, *Small* **2009**, *5*, 1688.
[25] S. Sańchez, L. Soler, J. Katuri, *Angew. Chem. Int. Ed.* **2015**, *54*, 1414.
[26] J. Li, I. Rozen, J. Wang, *ACS Nano* **2016**, *10*, 5619.
[27] W. Gao, S. Sattayasamitsathit, J. Wang, *Chem. Rec.* **2012**, *12*, 224.
[28] Y. Mei, A. A. Solovev, S. Sanchez, O. G. Schmidt, *Chem. Soc. Rev.* **2011**, *40*, 2109.
[29] H. Wang, M. Pumera, *Chem. Rev.* **2015**, *115*, 8704.
[30] M. P. Stoykovich, H. Kang, K. C. Daoulas, G. Liu, C. C. Liu, J. J. de Pablo, M. Müller, P. F. Nealey, *ACS Nano* **2007**, *1*, 168.
[31] J. Bang, U. Jeong, D. Y. Ryu, T. P. Russell, C. J. Hawker, *Adv. Mater.* **2009**, *21*, 4769.
[32] C. M. Bates, M. J. Maher, D. W. Janes, C. J. Ellison, C. G. Willson, *Macromolecules* **2013**, *47*, 2.
[33] C. H. Lin, S. Polisetty, L. O'Brien, A. Baruth, M. A. Hillmyer, C. Leighton, W. L. Gladfelter, *ACS Nano* **2015**, *9*, 1379.
[34] R. W. Johnson, A. Hultqvist, S. F. Bent, *Mater. Today* **2014**, *17*, 236.
[35] N. P. Dasgupta, H. B. R. Lee, S. F. Bent, P. S. Weiss, *Chem. Mater.* **2016**, *28*, 1943.
[36] H. Kim, H. B. R. Lee, W. J. Maeng, *Thin Solid Fims* **2009**, *517*, 2563.
[37] S. J. Ku, G. C. Jo, C. H. Bak, S. M. Kim, Y. R. Shin, K. H. Kim, S. H. Kwon, J. B. Kim, *Nanotechnology* **2013**, *24*, 085301.
[38] C. Sinturel, M. Vayer, M. Morris, M. A. Hillmyer, *Macromolecules* **2013**, *46*, 5399.
[39] J. Hong, J. B. Lee, S. Lee, J. Seo, H. Lee, J. Y. Park, J. H. Ahn, T. I. Seo, T. Lee, H. B. R. Lee, *NPG Asia Mater.* **2016**, *8*, e262.
[40] J. Li, G. Huang, M. Ye, M. Li, R. Liu, Y. Mei, *Nanoscale* **2011**, *3*, 5083.
[41] W. Gao, A. Pei, R. Dong, J. Wang, *J. Am. Chem. Soc.* **2014**, *136*, 2276.
[42] X. Ma, A. Jannasch, U. R. Albrecht, K. Hahn, A. Miguel-López, E. Schäffer, S. Sánchez, *Nano Lett.* **2015**, *10*, 7043.
[43] L. K. E. A. Abdelmohsen, M. Nijemeisland, G. M. Pawar, G.-J. A. Janssen, R. J. M. Nolte, J. C. M. van Hest, D. A. Wilson. *ACS Nano* **2016**, *10*, 2652.
[44] J. F. Brady, *J. Fluid Mech.* **2011**, *667*, 216.
[45] W. Wang, W. Duan, S. Ahmed, T. E. Mallouk, A. Sen, *Nano Today* **2013**, *8*, 541.
[46] W. Wang, W. Duan, S. Ahmed, A. Sen, T. E. Mallouk, *Acc. Chem. Res.* **2015**, *48*, 1938.
[47] A. A. Solovev, S. Sanchez, O. G. Schmidt. *Nanoscale* **2013**, *5*, 1284.
[48] B. Dai, J. Wang, Z. Xiong, X. Zhan, W. Dai, C.-C. Li, S.-P. Feng, J. Tang. *Nat. Nanotechnol.* **2016**, *11*, 1087.
[49] A. R. Morgan, A. B. Dawson, H. S. Mckenzie, T. S. Skelhon, R. Beanland, H. P. Franks, S. A. Bon, *Mater. Horiz.* **2014**, *1*, 65.
[50] B. Ezhilan, W. Gao, A. Pei, I. Rozen, R. Dong, B. Jurado-Sanchez, J. Wang, D. Saintillan, *Nanoscale* **2015**, *7*, 7833.